

Neutron flux evaluation algorithm with a combination of Monte Carlo and removal-diffusion calculation methods for boron neutron capture therapy

Mai Nojiri¹ | Takushi Takata² | Naonori Hu^{2,3} | Yoshinori Sakurai² |
Minoru Suzuki² | Hiroki Tanaka²

¹Department of Nuclear Engineering,
Graduate School of Engineering, Kyoto
University, Kyoto, Japan

²Institute for Integrated Radiation and Nuclear
Science, Kyoto University, Osaka, Japan

³Kansai BNCT Medical Center, Osaka
Medical and Pharmaceutical University,
Takatsuki, Osaka, Japan

Correspondence

Takushi Takata, Asashiro-nishi, Kumatori-cho,
Sennan-gun, Osaka 590-0494, Japan.
Email: takata.takushi.6x@kyoto-u.ac.jp

Funding information

JSPS KAKENHI, Grant/Award Number:
JP20K08078; JST SPRING, Grant/Award
Number: JPMJSP2110

Abstract

Background: In Japan, the clinical treatment of boron neutron capture therapy (BNCT) has been applied to unresectable, locally advanced, and recurrent head and neck carcinomas using an accelerator-based neutron source since June of 2020. Considering the increase in the number of patients receiving BNCT, efficiency of the treatment planning procedure is becoming increasingly important. Therefore, novel and rapid dose calculation algorithms must be developed. We developed a novel algorithm for calculating neutron flux, which comprises of a combination of a Monte Carlo (MC) method and a method based on the removal-diffusion (RD) theory (RD calculation method) for the purpose of dose calculation of BNCT.

Purpose: We present the details of our novel algorithm and the verification results of the calculation accuracy based on the MC calculation result.

Methods: In this study, the “MC-RD” calculation method was developed, wherein the RD calculation method was used to calculate the thermalization process of neutrons and the MC method was used to calculate the moderation process. The RD parameters were determined by MC calculations in advance. The MC-RD calculation accuracy was verified by comparing the results of the MC-RD and MC calculations with respect to the neutron flux distributions in each of the cubic and head phantoms filled with water.

Results: Comparing the MC-RD calculation results with those of MC calculations, it was found that the MC-RD calculation accurately reproduced the thermal neutron flux distribution inside the phantom, with the exception of the region near the surface of the phantom.

Conclusions: The MC-RD calculation method is useful for the evaluation of the neutron flux distribution for the purpose of BNCT dose calculation, except for the region near the surface.

KEYWORDS

boron neutron capture therapy, dose calculation algorithm, Monte Carlo method, removal-diffusion, treatment planning

This is an open access article under the terms of the [Creative Commons Attribution](https://creativecommons.org/licenses/by/4.0/) License, which permits use, distribution and reproduction in any medium, provided the original work is properly cited.

© 2024 The Authors. *Medical Physics* published by Wiley Periodicals LLC on behalf of American Association of Physicists in Medicine.

1 | INTRODUCTION

Boron neutron capture therapy (BNCT) is a type of radiotherapy that makes use of the nuclear reaction that occurs between a thermal neutron and a ^{10}B atom, which has a large thermal neutron absorption cross-section.¹ By accumulating the ^{10}B atoms inside the tumor cells prior to neutron irradiation, it can selectively kill the tumor cells and ensure minimal damage to the normal tissue. This is because the ranges of the alpha particle and ^7Li nuclei produced by the nuclear reaction are similar in size to those of human cells. In addition, it has a strong antitumor effect because the produced particles exhibit high linear energy transfer. Therefore, BNCT is expected to be effective in treating intractable tumors.² Furthermore, using epithermal neutrons, which have higher energy than thermal neutrons, makes it possible to treat deep-seated tumors, which is difficult to accomplish with thermal neutrons.³

In Japan, the clinical treatment of BNCT has been applied to unresectable, locally advanced, and recurrent head and neck carcinomas using accelerator-based neutron sources since June of 2020.^{4–8} Considering the increase in the number of patients receiving BNCT, treatment planning efficiency is becoming increasingly important. Treatment planning system for BNCT includes the NeuCure Dose Engine (Sumitomo Heavy Industries, Ltd), which is commercialized as medical equipment, and Tsukuba Plan developed by Kumada et al.^{9–11} The dose calculation code system implemented in these systems is Particle and Heavy Ion Transport code System (PHITS), a Monte Carlo (MC) code developed by Sato et al.¹² Recently, a novel treatment planning system, NeuMANTA, was developed and has a novel MC dose engine COMPASS.^{13,14} Only the MC method is currently used as the dose calculation algorithm in the treatment planning systems for the clinical treatment of BNCT. There is a need and demand to develop a faster dose calculation algorithm that can also be used for independent dose calculation.

Some studies have focused on the development of dose calculation algorithms for BNCT. Takada et al. calculated neutron flux distributions in a head and neck phantom by solving multi-group diffusion equations, which were made by dividing a continuous neutron energy into eight energy groups.¹⁵ The calculation time was shorter than that of the MC calculation but the calculation accuracy was low. In our previous study, we calculated the thermal neutron flux distribution by convolution-integrating isotropic kernels with the distribution of neutrons terminated below 1 eV.¹⁶ This method achieved a shorter calculation time than that of the MC method, and the calculations mostly reproduced the distribution in the deep region, compared with the MC calculation. However, it significantly overestimated the distribution in the shallow region. This was attributed to the lack of consideration of the neutrons escaping from the surface. Albertson and Niemkiewicz et al. suggested

the calculation method based on the removal-diffusion (RD) theory considering neutrons in the pre-collision process.^{17–19} Consequently, the calculation accuracy of thermal neutron flux distribution was high near the surface. However, they limited the evaluation for the neutron energy range below 0.3 MeV, which is below the maximum value (~ 28 MeV) of the energy used for the current clinical BNCT.^{5,8,17–19} In addition, they performed RD calculations only for the neutron energy below 0.3 MeV. At higher energies, it is difficult to establish the diffusion theory, and therefore the calculation accuracy will be lower. In addition, they conducted the calculation using only simplified geometry, such as semi-infinite geometry, ellipsoids, and cuboids, instead of the geometries close to the actual conditions.^{17–19}

In this study, we calculated the neutron flux inside a phantom with a shape resembling that used in the clinical treatment, using a combination of the MC and RD calculation methods based on RD theory, hereby known as the “MC-RD” calculation. The accuracy of the MC-RD calculation of neutron flux distribution was verified using cubic and head-shaped water phantoms.

2 | MATERIALS AND METHODS

In the MC-RD calculation method, neutron collision and scattering are divided into two processes: the moderation process, in which the incident neutrons reduce their energy by colliding with nuclei comprising the human body, and the thermalization process, in which the moderated neutrons reach thermal equilibrium with the nuclei. The neutron distributions are calculated for each process. The moderation and thermalization processes are simulated by MC and RD calculations, respectively.

The calculation accuracy was verified based on the results of the full-continuous-MC calculation, which adopts the MC method continuously for all neutrons, and the isotropic-thermal-MC calculation, which uses the MC method assuming that neutrons isotropically spread immediately after entering the thermalization process.

We further calculated the in-phantom neutron fluxes modeling the irradiation of the cubic and head-shaped phantoms filled with water. The neutron source used for the calculation was modeled to closely resemble the Heavy Water Neutron Irradiation Facility of Kyoto University Reactor (KUR-HWNIF), which has a neutron energy close to the energy range of epithermal neutrons.²⁰ The main types of neutrons and the corresponding energy ranges for BNCT are defined as follows: thermal neutrons with energy lower than 0.5 eV, epithermal neutrons with energy from 0.5 eV to 10 keV, and fast neutrons with energy above 10 keV.^{21,22} Since the MC method is used in both situations to compute the flux of neutrons with energy greater than 1 eV, the fast neutron flux distribution results for the MC-RD and full-continuous-MC computations are considered to be the same. Therefore, the accuracy of the MC-RD calculation for fast neutron flux is omitted.

In this study, the MC-RD calculation results of thermal and epithermal neutron flux distributions were compared with those of the full-continuous-MC and isotropic-thermal-MC calculations. MC calculations were conducted using the MC code PHITS, and the distributions were calculated using a mesh size of 3 mm.¹²

2.1 | MC-RD calculation

2.1.1 | RD theory and equations

The traditional diffusion theory only takes into account the “collided” neutrons, whereas the RD theory includes both the “uncollided” and the collided neutrons.^{17–19,23}

When calculating the neutron flux in the geometry shown in Subsection 2.2, the distribution $S_0(\mathbf{r}')$ of neutrons terminated below 1 eV in the phantom after being produced from the neutron source was derived using MC calculation with the cutoff function by setting the cutoff energy to 1 eV. $S_0(\mathbf{r}')$ was used as the source for the calculation of uncollided neutron fluxes.

The number of uncollided neutrons decreases as a function of the macroscopic total reaction cross-section for the material through which the neutrons pass. Therefore, the flux $\phi_{u,m}(\mathbf{r})$ of the uncollided neutrons in the energy group $m(m = 1, 2, 3, \dots)$ at position \mathbf{r} is obtained using the following equation:

$$\phi_{u,m}(\mathbf{r}) = \int \frac{S_{0,m}(\mathbf{r}') e^{-\Sigma_{ut,m}|\mathbf{r}-\mathbf{r}'|}}{4\pi|\mathbf{r}-\mathbf{r}'|^2} d\mathbf{r}', \quad (1)$$

where $S_{0,m}(\mathbf{r}')$ is the distribution of neutrons terminated in the energy range of group m in the phantom. As described in Equation (2), it is determined using $S_0(\mathbf{r}')$ and the source intensity ratio $C_m(0 < C_m < 1)$ for group m , which is derived from the spectrum calculated in Subsection 2.1.2.

$$S_{0,m}(\mathbf{r}') = C_m S_0(\mathbf{r}'). \quad (2)$$

$\Sigma_{ut,m}$ is the macroscopic total reaction cross-section, which depends on the energy spectrum of uncollided neutrons.

As described in Equation (3), the $\phi_{u,m}(\mathbf{r})$ is multiplied by the macroscopic scattering reaction cross-section $\Sigma_{us,m \rightarrow n}(n \geq m)$ in the process where neutrons moderate from the energy group m to n due to the collision with the material to derive the source intensity $S_{c,n}(\mathbf{r})$ for collided neutrons in the group n :

$$S_{c,n}(\mathbf{r}) = \Sigma_{us,m \rightarrow n} \phi_{u,m}(\mathbf{r}). \quad (3)$$

$\Sigma_{us,m \rightarrow n}$ depends on the energy spectrum of uncollided neutrons. Using $S_{c,n}(\mathbf{r})$, the flux $\phi_{c,n}(\mathbf{r})$ of collided neutrons in the group n is derived by solving the following

diffusion equation:

$$\begin{aligned} & -\nabla \cdot \{D_n(\mathbf{r}) \nabla \phi_{c,n}(\mathbf{r})\} + \Sigma_{cr,n} \phi_{c,n}(\mathbf{r}) \\ & = \sum_{m(<n)} \Sigma_{cs,m \rightarrow n} \phi_{c,m}(\mathbf{r}) + S_{c,n}(\mathbf{r}), \end{aligned} \quad (4)$$

where $\Sigma_{cr,n}$ is the macroscopic reaction cross-section in the process where the collided neutron is removed from group n by down-scattering to group $l(l > n)$ from n or by absorption in the group n , as shown in the following equation:

$$\Sigma_{cr,n} = \Sigma_{ca,n} + \sum_{l(>n)} \Sigma_{cs,n \rightarrow l}. \quad (5)$$

$D_n(\mathbf{r})$ is the diffusion coefficient for the neutrons in group n . In this study, $D_n(\mathbf{r})$ is constant at position \mathbf{r} because the material related to the diffusion equation is only water, which is homogeneously filled in the phantom. Therefore, Equation (4) is simplified to the following equation:

$$-D_n \Delta \phi_{c,n}(\mathbf{r}) + \Sigma_{cr,n} \phi_{c,n}(\mathbf{r}) = \sum_{m(<n)} \Sigma_{cs,m \rightarrow n} \phi_{c,m}(\mathbf{r}) + S_{c,n}(\mathbf{r}). \quad (6)$$

The diffusion Equation (6) can be discretized and transformed into three-dimensional difference equations. The $\phi_{c,n}(\mathbf{r})$ is derived by solving the difference equations.

Finally, the total neutron flux $\phi(\mathbf{r})$ is derived by summing $\phi_u(\mathbf{r})$ and $\phi_c(\mathbf{r})$ in each energy group as follows:

$$\phi(\mathbf{r}) = \phi_u(\mathbf{r}) + \phi_c(\mathbf{r}). \quad (7)$$

The MC calculation for the moderation process was conducted by setting the cutoff energy as 1 eV to derive the distribution of the neutrons terminated below 1 eV in the phantom and the flux distribution of epithermal neutrons with the energy between 1 eV and 10 keV. The RD calculation for the thermalization process was conducted following Equations (1)–(7) by dividing the neutrons with energies below 1 eV into two energy groups: neutrons with energies between 0.5 and 1 eV were placed in group 1, and neutrons with energies below 0.5 eV were placed in group 2. Diffusion equations for the energy groups were set up and solved to derive the neutron fluxes. The neutron flux in group 2 was determined to be the thermal neutron flux. The epithermal neutron flux was determined by summing the fluxes of the neutrons in group 1 and neutrons with energies between 1 eV and 10 keV. The calculation flow is illustrated in Figure 1. In addition, a glossary for the terms used in Equations (1)–(7) can be found in the Appendix.

2.1.2 | Spectrum of neutrons terminated below 1 eV

The energy spectrum of neutrons terminated below 1 eV was calculated as the first step for determining the parameters of the macroscopic reaction cross-sections,

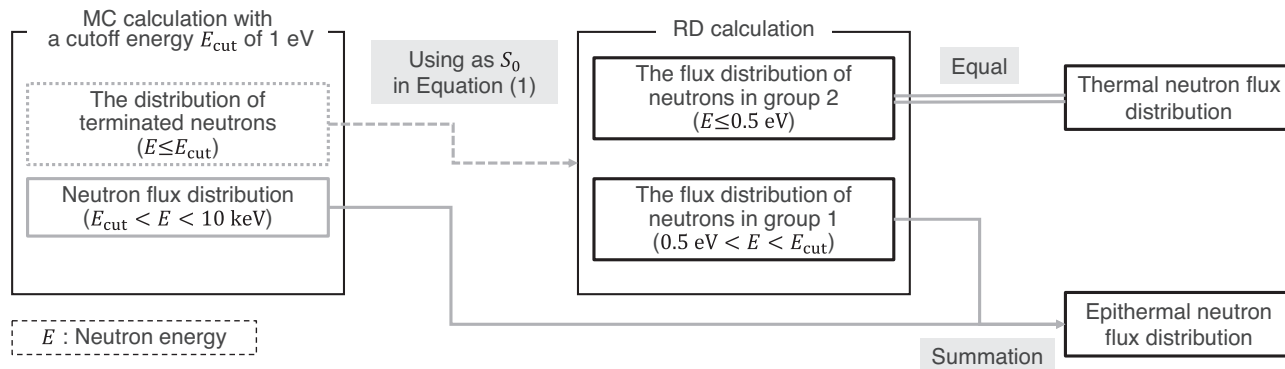


FIGURE 1 MC-RD calculation flow. The calculation accuracy of the distribution surrounded by the thick black frame was verified.

diffusion coefficients, extrapolation distances, and the ratio of source intensities of neutron energy groups 1 and 2, which are required for the RD calculation. The neutron spectra terminated below 1 eV in the phantom were calculated using depth intervals of 0.5 cm between 0.25 and 6.25 cm along the central axis for both the cubic and head-shaped phantoms filled with water. The spectra were then averaged to derive the spectrum in each geometry. As described in our previous study, these spectra were estimated to be independent of the geometry and the depth on the beam central axis.¹⁵ The spectrum was divided into spectra in groups 1 and 2. The cross-sections, diffusion coefficients, and extrapolation distances were estimated for each group in the geometry, wherein each spectrum was set as the source, as shown in Subsections 2.1.3 and 2.1.4.

2.1.3 | Macroscopic reaction cross-sections

The macroscopic absorption and scattering reaction cross-sections were determined using a water sphere with a radius of 4 cm, as shown in Figure 2. The point source with the energy spectrum of neutrons in each energy group was set at the center of the sphere to determine the cross-sections of neutrons in each energy group.

The macroscopic absorption reaction cross-section $\Sigma_{ua,m}$ of uncollided neutrons in group m was determined as follows. The absorption reaction rate $R_{ua,m}$ of the uncollided neutron for ^1H and the uncollided neutron flux $\phi'_{u,m}$ were calculated for neutrons in group m , and $R_{ua,m}$ was divided by $\phi'_{u,m}$ to determine $\Sigma_{ua,m}$. The absorption reaction cross-section $\Sigma_{ca,m}$ of the collided neutrons in group m was obtained in the same manner. The absorption reaction cross-sections for ^1H only were used as the cross-sections $\Sigma_{ua,m}$ and $\Sigma_{ca,m}$ for water because the absorption by ^1H was attributed to the calculation result.

The macroscopic cross-section $\Sigma_{us,m \rightarrow n}$ of the scattering reaction from the energy group m to n for uncollided neutrons was determined as follows. The reaction rate $R_{us,m \rightarrow n}$ of scattering from the energy

group m to n after the first collision and $\phi'_{u,m}$ were calculated, and $R_{us,m \rightarrow n}$ was divided by $\phi'_{u,m}$ to determine $\Sigma_{us,m \rightarrow n}$. The energy spectrum of neutrons after the first collision was calculated in each spherical shell surrounded by the outer and inner surfaces with radii increasing with intervals of 1 mm. The spectra in the region, except for the source position and the edge of the sphere, were averaged to derive the spectrum of collided neutrons. Using the source with the spectrum, the macroscopic cross-section $\Sigma_{cs,m \rightarrow n}$ of the scattering reaction from the energy group m to n for collided neutrons was determined by a process similar to the determination of $\Sigma_{us,m \rightarrow n}$.

These calculations were conducted using PHITS ver. 3.24 and JENDL-4.0 (the fourth version of Japanese Evaluated Nuclear Data Library).^{12,24,25} The reaction rate was calculated using the [T-Track] and [Multiplier] tally functions, and the neutron flux was calculated using the [T-Track]. The uncollided and collided neutrons were distinguished by using the [Counter] tally. The scattering reaction rate in each collision was calculated using [Counter] and [T-Product] tallies. [Counter] allows storing the increment of the counter of the particle when a scattering reaction occurs in the track of the particle. In the calculation using [T-Track], uncollided and collided neutrons were discriminated by selecting the particle to score whose value corresponded to the value of the counter. In the calculation using [T-Product], the first collisions of neutrons were captured by a process similar to that in the calculation using [T-Track].

Finally, the total reaction cross-sections $\Sigma_{ut,m}$ and $\Sigma_{ct,m}$ in energy group m were determined by summing the absorption and scattering cross-sections in the group.

2.1.4 | Diffusion coefficient and extrapolation distance

Diffusion coefficients D_n and extrapolation distances ϵ_n were determined for each neutron energy group. Here, the extrapolation distance is the distance from the boundary between the material and the void (or air) to

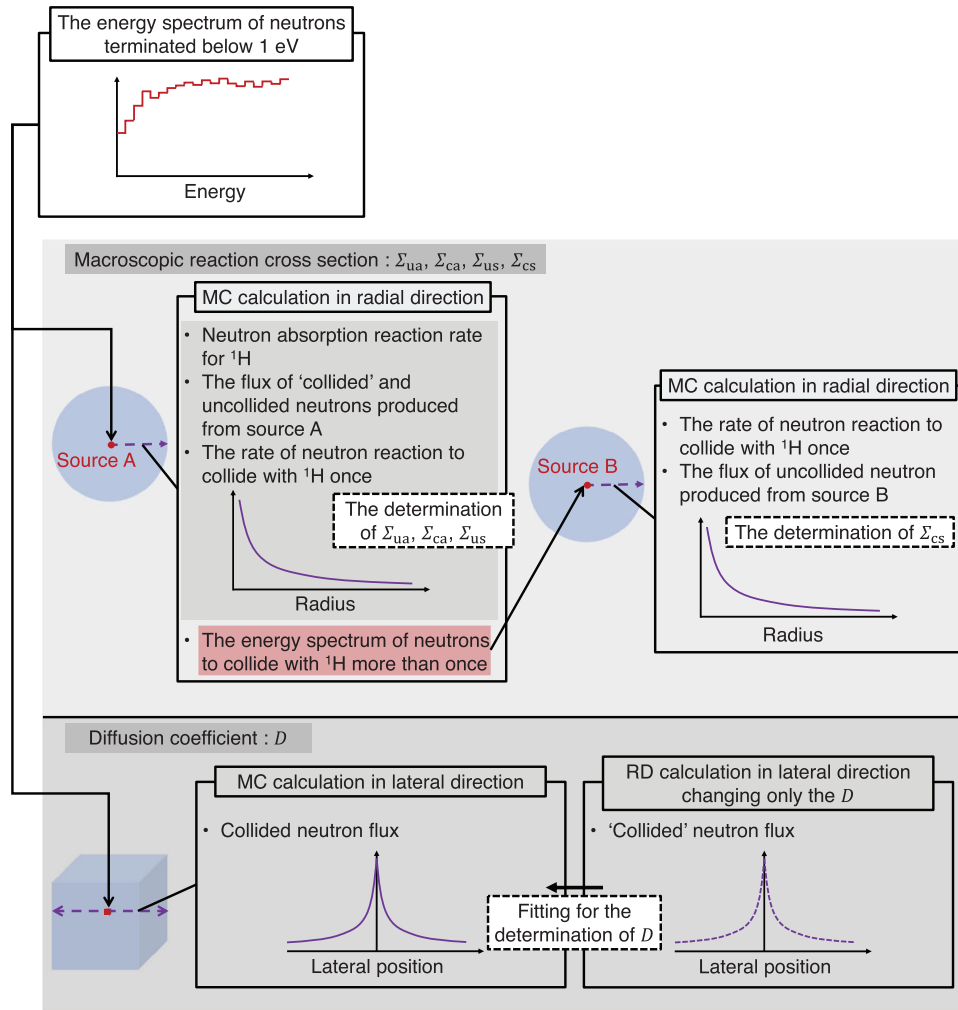


FIGURE 2 Determination of cross-sections and diffusion coefficients. The macroscopic reaction cross-section and diffusion coefficient were determined using the geometry setting the energy spectrum of neutrons terminated below 1 eV as the source. The macroscopic cross-section was determined by the calculation in the geometry where the point source was set at the center of the water sphere. The radial distribution of neutron absorption reaction rates, neutron fluxes, and the reaction rate in the first collision of neutrons were calculated to determine the neutron absorption reaction cross-section and the uncollided neutron scattering reaction cross-section. The energy spectrum of neutrons that collide more than once was also calculated as the source in the geometry to determine the scattering reaction cross-section for the collided neutrons. Diffusion coefficients were determined by the calculation in the geometry where the cubic source was set at the center of the cubic water region. The collided neutron flux was calculated to determine the diffusion coefficient by fitting the MC-RD calculation results to the MC calculation results using only the diffusion coefficient.

the pseudo-determined position, where the neutron flux reaches zero. D_n and ϵ_n are defined using the mean free path λ_{tr} as follows²⁶:

$$D_n = \frac{\lambda_{tr}}{3}, \tag{8}$$

$$\epsilon_n = 0.7104\lambda_{tr}. \tag{9}$$

Therefore, ϵ_n is estimated using D_n as follows:

$$\epsilon_n = 0.7104 \times 3 \times D_n. \tag{10}$$

D_n was determined by fitting the results of the calculation based on Equations (1)–(6) to the MC calculation

results based on the collided neutron flux distribution. Generally, on the condition that the movement of atomic nuclei bound by water molecules is negligible in the simulation of the collision and scattering processes of neutrons, λ_{tr} can be derived using the total reaction and total scattering reaction cross-sections. However, in the calculation for the thermalization process, the derivation of λ_{tr} is more complex because the movement of nuclei in water molecules cannot be ignored. Therefore, D_n was determined by fitting RD calculation results to the results of MC calculation using PHITS. The fitting parameter can only be D_n because ϵ_n was determined based on D_n using Equation (10). Here, the glossary for the terms used in Equations (8)–(10) can also be found in the Appendix.

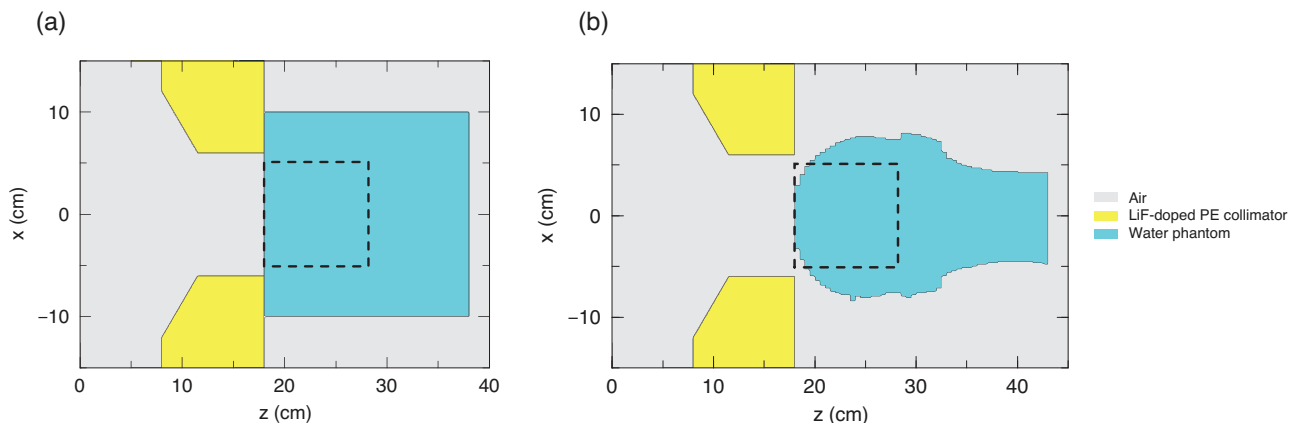


FIGURE 3 Cross-section views of (a) cubic and (b) head-shaped water phantoms. Neutrons with energies higher than 1 eV were tallied at the circular surface including the downstream surface of the LiF-doped PE collimator. The two-dimensional distribution in the region surrounded by the dotted line is demonstrated in the Results section.

After determining the cross-sections as shown in Section 2.1.3, the collided neutron flux distribution $\phi'_{c,n}(\mathbf{r})$ was calculated based on Equations (1)–(6) in rectangular coordinates with a mesh size of 3 mm. The fitting was conducted using a geometry such that the source with a side of 3 mm was set at the center of the cubic water region, with a side distance of 12.3 cm. This allows the geometry to be divided into calculation meshes in rectangular coordinates. The fitting target region was set such that the region where the source position was and the region comprising the positions three times larger than λ_{tr} from the edge were excluded. In addition, the flux distribution of collided neutrons in the same energy group as the source was used for the fitting by setting the first term $\sum_{m(<n)} \Sigma_{cs,m \rightarrow n} \phi_{c,m}(\mathbf{r})$ on the right side of Equation (6) to zero, limiting the number of fitting parameters to one.

ϵ_n was determined from D_n using Equation (10). However, the estimated ϵ_n changed depending on the calculation mesh size M in the numerical calculation. When ϵ_n was larger than or equal to pM and less than $(p+1)M$ for $p = 0, 1, 2, \dots$, ϵ_n could be changed to the following ϵ'_n :

$$\epsilon'_n = pM. \quad (11)$$

2.2 | Calculation geometry and source

MC-RD calculations using cubic and head-shaped water phantoms were used to verify the calculation accuracy. As shown in Figure 3a, a cubic phantom with a geometry of $20 \times 20 \times 20 \text{ cm}^3$ was modeled using PHITS. As shown in Figure 3b, the head-shaped voxel-phantom was modelled based on the CT images of the head phantom, with the composition set to water. The collimator (LiF-doped PE) has a circular aperture with a diameter of 12 cm.

The calculation accuracy was verified by setting the dump source of neutrons with energies larger than 1 eV on the surface between the collimator and phantom. In the MC-RD calculation, the in-phantom distribution of neutrons terminated below 1 eV was used. Therefore, neutron sources below 1 eV was not considered for the calculation. However, in current applications of clinical treatment of BNCT, the contribution is expected to be small because the accelerator-based neutron source does not contain many neutrons with energy below 1 eV.^{4–8}

The dump source was generated as follows. First, the source with a spectrum in the epithermal neutron irradiation field of KUR was set on the upstream side of the collimator, and the material on the downstream side of the collimator was set as void. Then, the dump source was created using the MC calculation, tallying the energy, position, and momentum of neutrons with energies larger than 1 eV at the circular surface with a radius of 45 cm, including the downstream side surface of the collimator. The statistical uncertainty of the surface source finally used for the calculations was $\sim 0.01\%$ for the entire region of the circular surface.

2.3 | Isotropic-thermal-MC calculation

In the MC-RD calculation, the distribution of neutrons that are terminated below 1 eV in the phantom after being produced from the neutron source, was used as $S_0(\mathbf{r}')$ in Equation (1), and $S_0(\mathbf{r}')$ was assumed to be an isotropic source. The isotropic-thermal-MC calculation was conducted following the assumption to confirm the other systematic factor related to the difference between the MC-RD calculation and the full-continuous-MC calculation results.

The isotropic-thermal-MC calculation was conducted as follows: The dump source of neutrons terminated

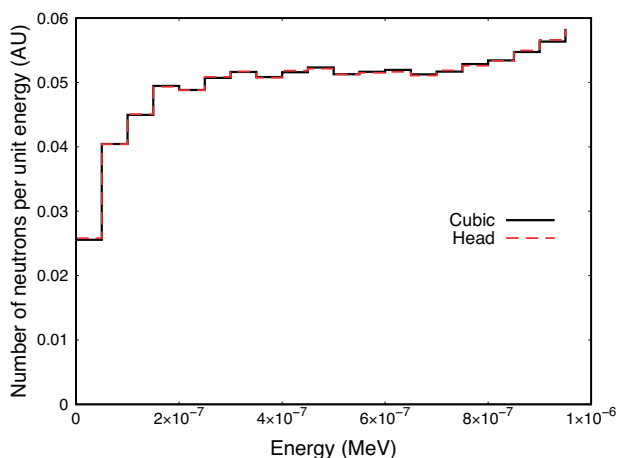


FIGURE 4 Energy spectra of neutrons terminated below 1 eV in the cubic and head-shaped water phantoms.

below 1 eV in the phantom was generated by the MC calculation using [T-Time] and dump mode implemented in PHITS.²⁴ The dump source information included the energy, position, and momentum of each terminated neutron. The neutron flux calculation was conducted isotropically producing neutrons from the dump source whose sampling in terms of the direction of movement was changed to an isotropic direction. In addition, the dump source was set in a geometry that included only the phantom. The numerical calculation for the thermalization process in MC-RD calculation did not consider the scatter structure, including the collimator. Therefore, the isotropic-thermal-MC calculation was conducted using the geometry, including only the phantom without the scatter structure. Notably, the effect of the scatter structure, including the collimator, was minimal and not primarily responsible for the variation from the full-continuous-MC calculation result.

The statistical uncertainties of the generated dump source of neutrons terminated below 1 eV were less than 0.01% in the phantom region for each of the cubic and head-shaped phantoms.

3 | RESULTS

3.1 | Spectra of neutrons terminated below 1 eV

Figure 4 shows the energy spectra of neutrons terminated below 1 eV in the beam central axis of the cubic and head-shaped water phantoms, which were derived by MC calculation with a cutoff energy of 1 eV. The maximum statistical uncertainty of the spectra before being averaged was less than 3%. Figure 4 shows that the spectra calculated using both cubic and head-shaped phantoms were similar. Our previous research also revealed that the spectrum does not depend on the

shape of the phantom.¹⁶ The neutron spectrum calculated using the cubic phantom was used as the neutron source for the determination of cross-sections, diffusion coefficients, extrapolation distances, and the ratio of source intensities of neutron energy groups 1 and 2 that are required for the RD calculation.

3.2 | Determined parameters for the RD calculation

Table 1 shows the parameters used for the RD calculation. The cross-sections and diffusion coefficients were estimated using the calculation described in Subsections 2.1.3 and 2.1.4, using the spectrum of neutrons terminated below 1 eV in the cubic phantom shown in Figure 4 in Subsection 3.1. The extrapolation distances were determined from the diffusion coefficients using Equation (10). However, the extrapolation distances change depending on the calculation mesh size following Equation (11) in the numerical calculation.

The statistical uncertainties of the results of the calculation using PHITS to determine the cross-section were less than 4%. The uncertainties of the results to determine the diffusion coefficient were less than 0.4%.

3.3 | Comparison of neutron flux distributions

In terms of the neutron fluxes in each energy group and epithermal neutron, the distribution derived through MC-RD calculation was mostly consistent with the full-continuous-MC and isotropic-thermal-MC calculation results for both the cubic and head-shaped phantoms, as shown in Figures 5–8. Figures 5 and 6 show the neutron flux distribution in the cubic water phantom, and Figures 7 and 8 show them in the head-shaped water phantom.

Figure 5a1 shows the depth distribution of the flux of thermal neutrons in the energy group 2 for the depths below 10 cm along the beam central axis of the cubic water phantom. Figure 5a2 shows the depth distribution of differences of the MC-RD calculation result for the full-continuous-MC and the isotropic-thermal-MC calculation results. Compared with the full-continuous-MC calculation values, the MC-RD calculation values were higher by approximately 16% for the depths below 1 cm and lower by approximately 9% for the deeper region. In addition, compared with the isotropic-thermal-MC calculation values, they were higher by approximately 20% for the depths below 2 cm and mostly consistent within 3% for the deeper region. For the two-dimensional distribution, as shown in Figure 5b, the MC-RD calculation result had values higher than both the results of full-continuous-MC and isotropic-thermal-MC calculations at the shallow region. For the deep region, the

TABLE 1 Values of parameters used for the RD calculation. The values in each row were determined for uncollided and collided neutrons (as indicated in parentheses). In the columns, in terms of the macroscopic cross-section, the absorption, scattering to stay in the energy group m , scattering from the energy group m to n , and total reaction cross-sections are shown from the left column.

Energy group	Macroscopic reaction cross-section (cm^{-1})			Diffusion coefficient (cm)	Extrapolation distance (cm)
	Absorption	Scattering ($m \rightarrow m$)	Scattering ($m \rightarrow n$)		
Group 1 (uncollided)	4.10×10^{-3}	7.62×10^{-1}	8.38×10^{-1}	1.60	—
Group 2 (uncollided)	6.69×10^{-3}	1.87	—	1.88	—
Group 1 (collided)	4.39×10^{-3}	6.47×10^{-1}	9.74×10^{-1}	1.63	3.84×10^{-1}
Group 2 (collided)	1.83×10^{-2}	2.43	—	2.45	1.50×10^{-1}

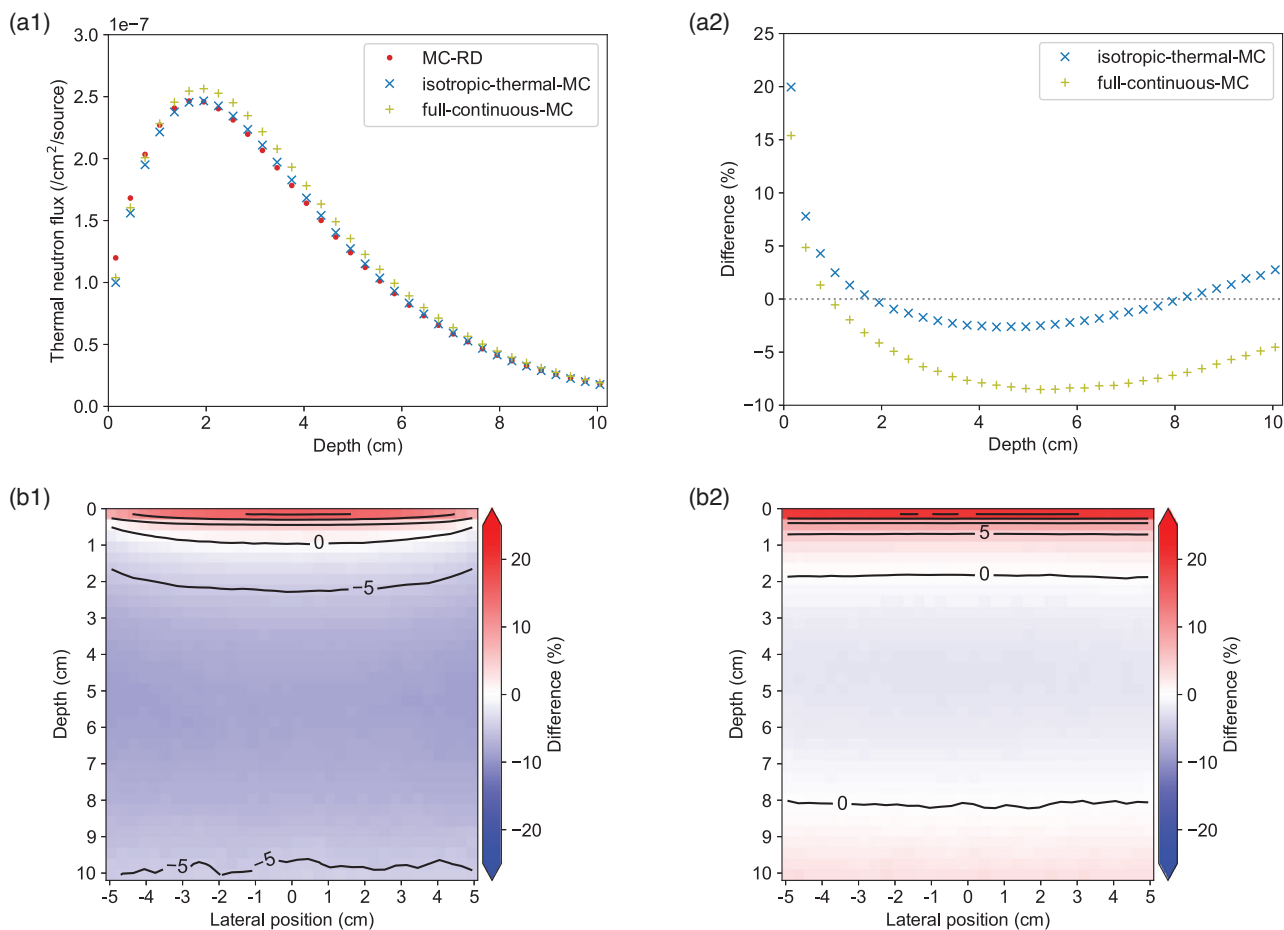


FIGURE 5 Comparison of thermal neutron flux distributions in the cubic phantom. (a1) Depth distributions derived by MC-RD, isotropic-thermal-MC, and full-continuous-MC calculations, (a2) depth distributions of differences of MC-RD calculation result for full-continuous-MC and isotropic-thermal-MC calculation results, and (b) two-dimensional distributions of differences of MC-RD calculation result for (b1) full-continuous-MC and (b2) isotropic-thermal-MC calculation results. The contour lines are drawn on the points with same differences at intervals of 5%, and the values are described on some lines.

MC-RD calculation result had values lower than the full-continuous-MC calculation and consistent with the isotropic-thermal-MC calculation.

Figure 6a1 shows the depth distribution of the neutron flux in energy group 1 at depths below 10 cm along the beam central axis. Figure 6a2 shows the difference in the depth distribution of the MC-RD calculation result for the full-continuous-MC and the isotropic-thermal-MC

calculation results. Compared with the full-continuous-MC calculation values, the MC-RD calculation values were higher by approximately 8% for the depths below 0.5 cm and lower by approximately 20% for the deeper region. In addition, compared with the isotropic-thermal-MC calculation values, they were lower by approximately 7% at depths below 1 cm and mostly consistent within 4% for the deeper region. Figure 6b1 shows

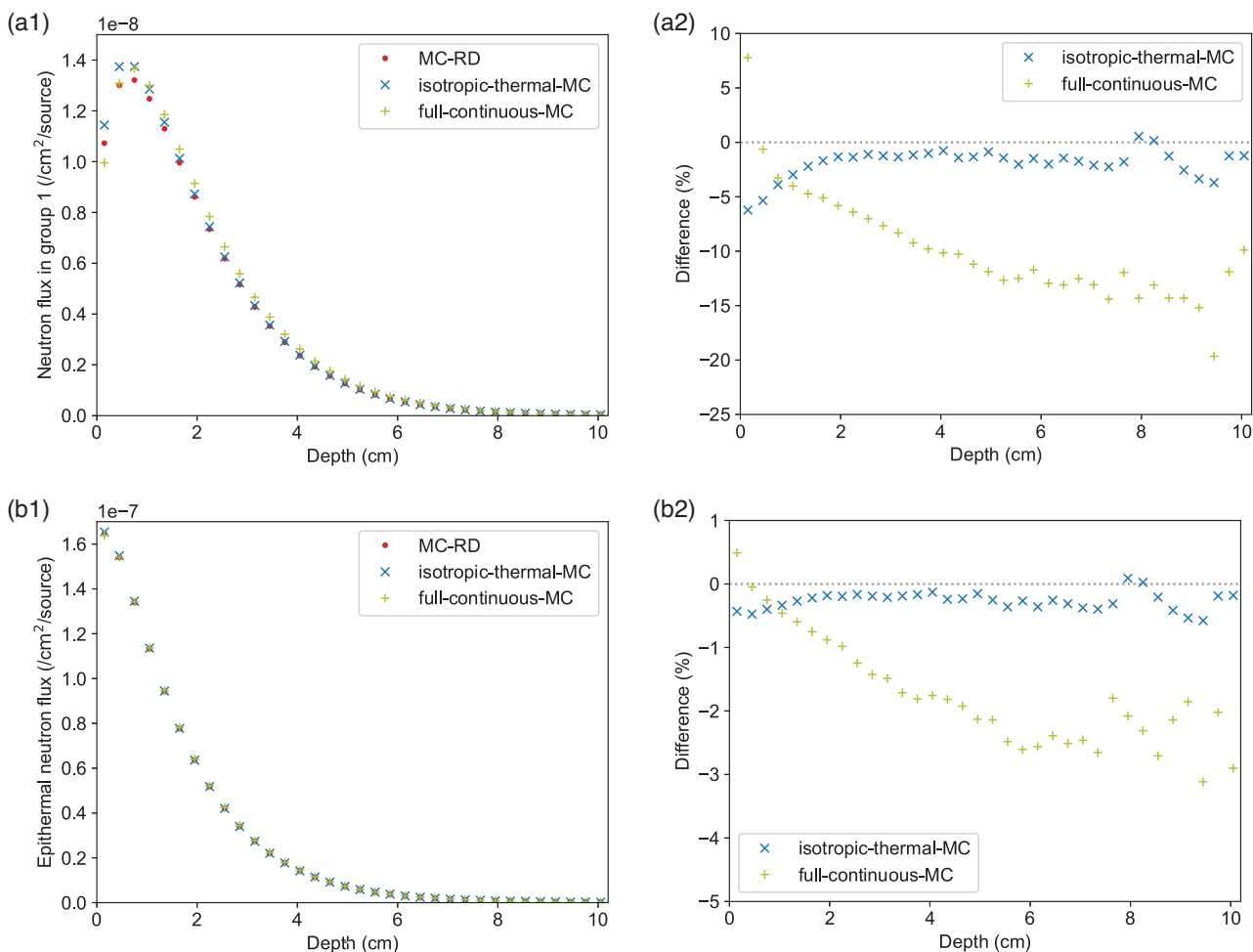


FIGURE 6 Comparison of flux distribution of (a) neutrons in energy group 1 and (b) epithermal neutrons in the cubic phantom. (a1, b1) The depth distributions derived by MC-RD, isotropic-thermal-MC, and full-continuous-MC calculations, (a2, b2) depth distributions of differences of MC-RD calculation results for full-continuous-MC and isotropic-thermal-MC calculation results.

the comparison of the depth distribution of the epithermal neutron flux including the flux of neutrons in the energy group 1. Figure 6b2 shows the differences in the depth distribution of the MC-RD calculation result for the full-continuous-MC and the isotropic-thermal-MC calculation results. The MC-RD calculation values exhibited mostly high consistency within 4% with the full-continuous-MC calculation values and within 1% with the isotropic-thermal-MC calculation values.

Figure 7a1 shows the depth distribution of thermal neutron flux in the neutron energy group 2 at depths below 10 cm along the beam central axis of the head-shaped water phantom. Figure 7a2 shows the difference in the depth distribution of the MC-RD calculation result for the full-continuous-MC and the isotropic-thermal-MC calculation results. Compared with the full-continuous-MC calculation values, the MC-RD calculation values were higher by approximately 19% at depths below 1.5 cm and lower by approximately 8% for the deeper region. In addition, compared with

the isotropic-thermal-MC calculation values, they were higher by approximately 21% at depths below 3 cm and in a mostly good agreement within 2% in the deeper region. Moreover, as shown in Figure 7b, the MC-RD calculation result had higher values than both results of full-continuous-MC and isotropic-thermal-MC calculations for the shallow region also in the two-dimensional distributions. In the deep region, the MC-RD calculation result had lower values than the full-continuous-MC calculation result and were consistent with the isotropic-thermal-MC calculation result.

Figure 8a1 shows the depth distribution of the neutron flux in the neutron energy group 1 for the depths below 10 cm along the beam central axis. Figure 8a2 shows the difference in the depth distribution of the MC-RD calculation result for the full-continuous-MC and the isotropic-thermal-MC calculation results. Compared with the full-continuous-MC calculation values, the MC-RD calculation values were higher by approximately 9% at depths below 0.5 cm and lower by

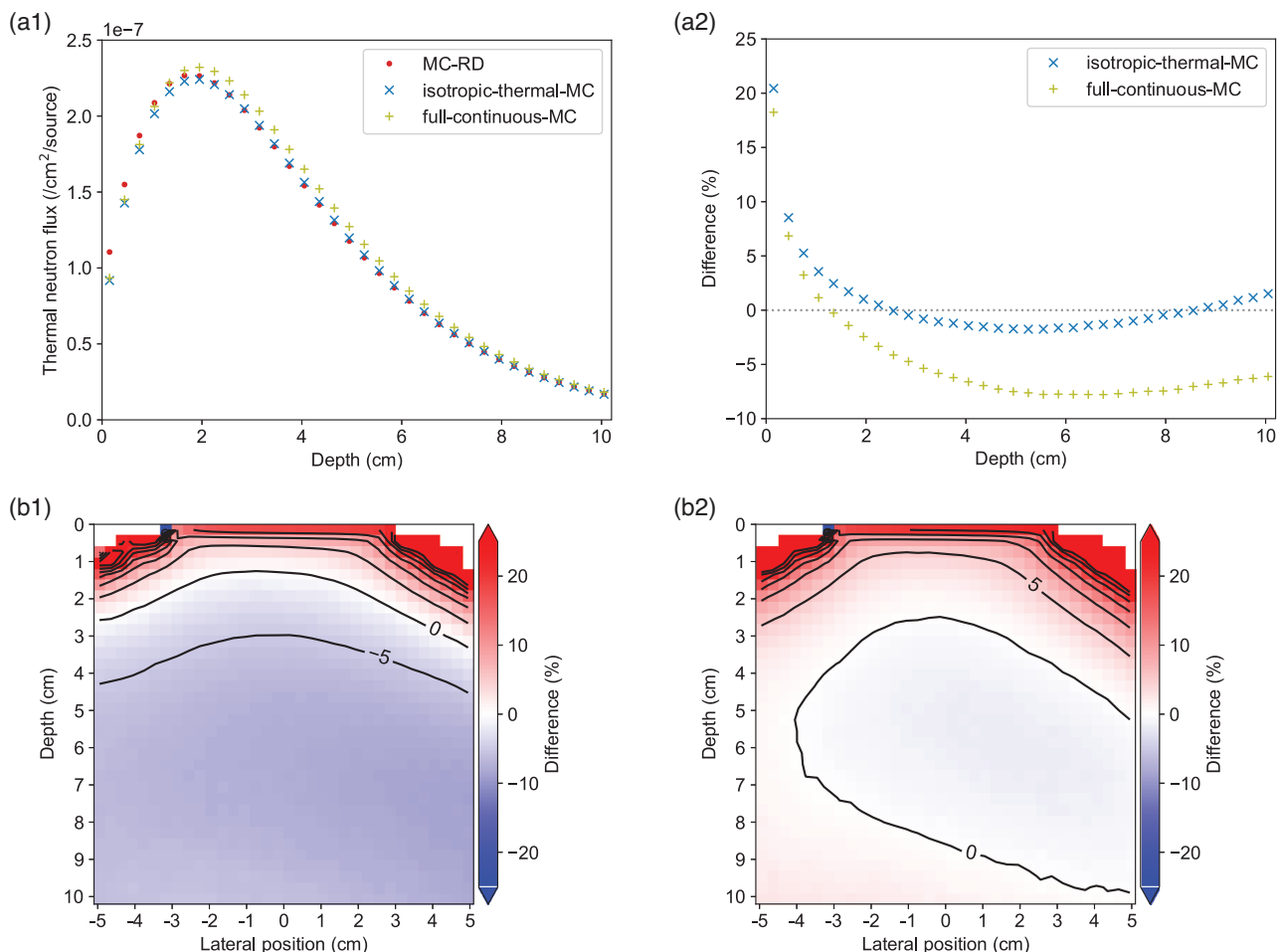


FIGURE 7 Comparison of thermal neutron flux distributions in the head-shaped phantom. (a1) The depth distributions derived by MC-RD, isotropic-thermal-MC, and full-continuous-MC calculations, (a2) depth distributions of differences of MC-RD calculation result for full-continuous-MC and isotropic-thermal-MC calculation results, and (b) two-dimensional distributions of differences of MC-RD calculation result for (b1) full-continuous-MC and (b2) isotropic-thermal-MC calculation results. The contour lines are drawn on the points with the same differences at intervals of 5%, and the values are described on some lines.

approximately 15% for the deeper region. In addition, compared with the isotropic-thermal-MC calculation values, they were lower by approximately 7% at depths below 2 cm and mostly consistent within 4% for the deeper region. Figure 8b1 shows the comparison of the depth distribution of the epithermal neutron flux including the flux of neutrons in energy group 1. Figure 8b2 shows the depth distribution of differences of the MC-RD calculation result for the full-continuous-MC and the isotropic-thermal-MC calculation results. The MC-RD calculation result exhibited mostly high consistent within 5% with the full-continuous-MC calculation result and within 1% with the isotropic-thermal-MC calculation result.

4 | DISCUSSION

In this study, we proposed the MC-RD calculation method that utilizes the MC calculation for the mod-

eration process of neutrons and the RD calculation for the thermalization process. The accuracy of the MC-RD calculation was verified based on the results of the full-continuous-MC calculation adopting the MC method continuously for full neutron energy and the isotropic-thermal-MC calculation based on the assumption that the neutrons isotropically spread immediately after entering the thermalization process.

The extrapolation distance was calculated using Equation (10). The value of 0.7104 used in the equation was determined for the planar boundary. The extrapolation distance can be increased and reaches $\frac{4}{3}\lambda_{tr}$ for boundary surfaces with higher curvatures.²⁶ Therefore, the accuracy of the calculation for the head-shaped phantom with a complex boundary surface could be affected by the extrapolation distance determined for the flat boundary surface. The phantom's shape was found to have an impact on the trends of disparities between the MC-RD and MC calculation results. But comparing Figures 5 and 7 shows that the trends were similar.

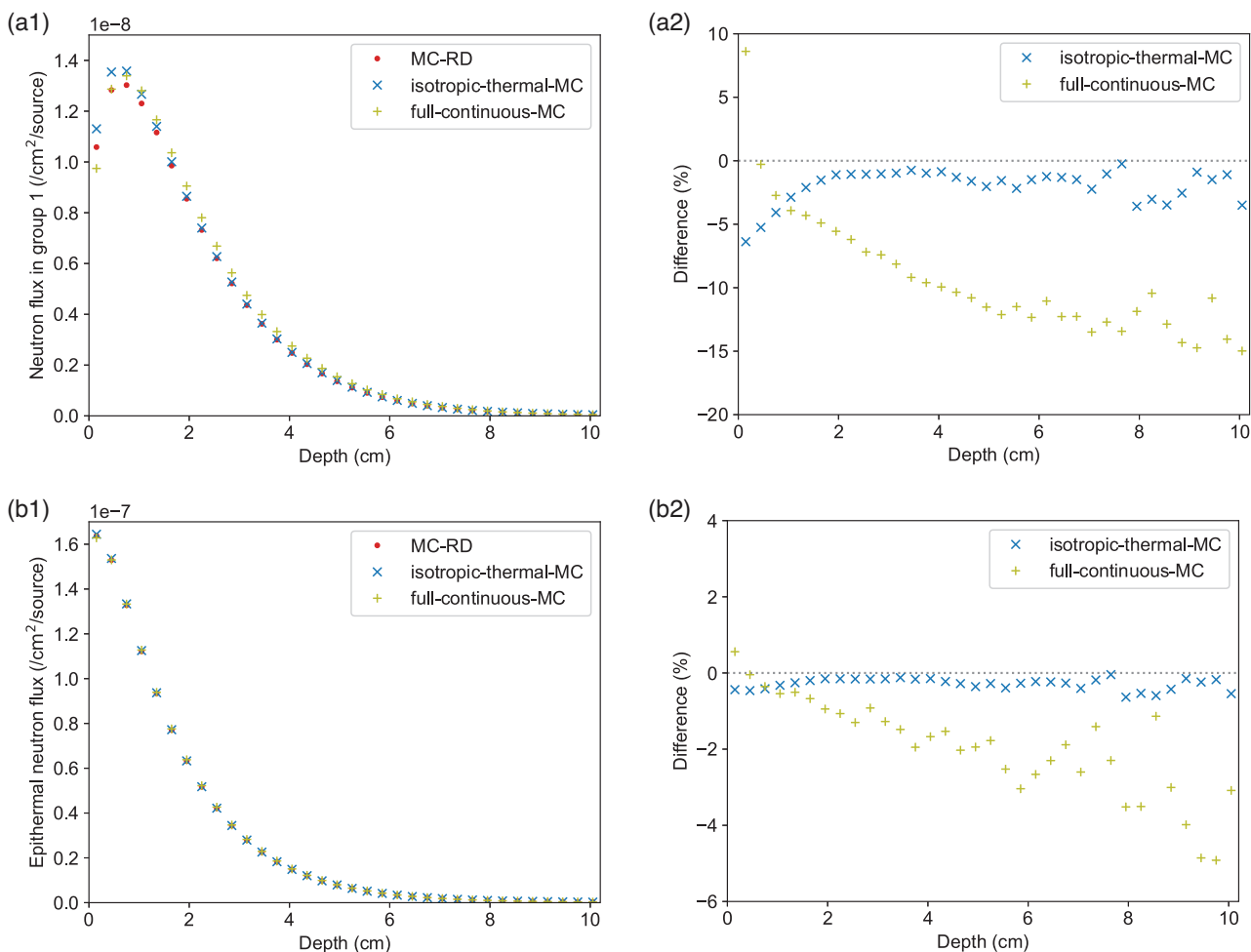


FIGURE 8 Comparison of flux distribution of (a) neutrons in energy group 1 and (b) epithermal neutrons in the head-shaped phantom. (a1, b1) The depth distributions derived by MC-RD, isotropic-thermal-MC, and full-continuous-MC calculations, (a2, b2) depth distributions of differences of MC-RD calculation results for full-continuous-MC and isotropic-thermal-MC calculation results.

Therefore, we cannot confirm the effect attributed to the difference in curvature of the boundary surface.

One of the factors that lead to the difference between the MC-RD and the full-continuous-MC calculation results can be elucidated based on the difference between the isotropic-thermal-MC and the full-continuous-MC calculation results. It was the assumption that neutrons spread isotropically immediately after entering the thermalization process. In fact, the direction of movement of the neutrons is considered to tend to take the downstream direction, especially near the surface of the phantom. The uncollided neutrons in the energy group 1 may be especially susceptible to this trend, since their angle distribution tends to follow the direction of irradiation at energies close to 1 eV. Furthermore, the number of in-phantom neutrons moving from the deep region to the shallow region and neutrons leaking from the phantom to the surface was considered to increase, compared to that in the full-continuous-MC calculation. Figures 6a and 8a illustrate how the overestimation of the fluxes in energy group 1 occurred in the shallow region, depending on the balance of the num-

bers, while Figures 5 and 7 illustrate the slight effect on the fluxes in energy group 2. In addition, the number of in-phantom neutrons moving from the shallow region to the deep region decreased because neutrons moving to the downstream direction were forced to move to the upstream direction in the MC-RD and isotropic-thermal-MC calculations, and the neutron flux distribution in the deep region was made up of neutrons terminated below 1 eV in the shallow region. Therefore, the underestimation of the fluxes in the energy groups 1 and 2 occurred in the deep region.

Under the assumption that neutrons isotropically spread immediately after entering the thermalization process, the MC-RD calculation overestimated the thermal neutron flux distribution obtained using the isotropic-thermal-MC calculation near the surface of the phantom. Similar trends appeared in the comparison of the two-dimensional distributions. This was considered to be attributed to the effect of diffusion approximation of the diffusion equation. In the diffusion approximation, the angular distribution of the neutron current was represented by the low-order angular approximation. The RD

calculation, in which the uncollided neutron distribution was used to determine the source term, could reduce the effect of diffusion approximation. However, this effect could not be eliminated completely.

In this study, the accuracy of the MC-RD calculation method was verified by focusing on neutron flux distributions inside a water phantom. To use this method as a treatment planning tool for clinical BNCT, it is necessary to take into account the components of the human body. By providing the ideal parameters for use in the RD calculations, such as the cross-section and diffusion coefficient, the MC-RD calculation may also be used to calculate the distributions inside a human body. These parameters can be prepared by using a simplified phantom composed of each of tumor and human tissues such as brain, bone, and soft tissue, following the determination process shown in Figure 2 and described in Subsections 2.1.3 and 2.1.4. Thereafter, the distributions can be derived via the RD calculations using the prepared parameters, from the process shown in Figure 1. Nevertheless, the components of the human body would not significantly affect the accuracy of the MC-RD calculation because the parameters would not significantly change between tissue types. However, the difference between the MC-RD calculation and the full-continuous-MC calculation results can occur near the region filled with air inside the body, such as the paranasal sinus and lung, in addition to the surface, because of the limitation in the diffusion approximation described above. However, the magnitude of the difference is predicted to be lower than the difference at the surface, shown in Figures 7 and 8 and described in the Results section, because the inner air region is surrounded with tissue.

As described above, the verification of the accuracy of the MC-RD calculation demonstrated that the calculation accuracy was affected by the assumption regarding the isotropic distribution of neutrons immediately after entering the thermalization process and the limitation of diffusion approximation. In addition, the calculations were conducted with the mesh size set to 3 mm. The calculation with a bigger mesh cannot accurately consider the extrapolation distance, thus decreasing the calculation accuracy.

However, the epithermal and fast neutron flux calculations have an accuracy level comparable to that of the MC calculation, because the moderation process in this study was carried out using the MC calculation. As mentioned in the introduction, Takada et al. only employed the diffusion equation for the calculation, and Albertson and Niemkiewicz et al. only conducted the RD calculation for neutrons with lower energy compared to the source currently used for BNCT.^{15,17–19} The calculation accuracy of their methods can be low for the fast neutrons. Furthermore, the thermal neutron flux in the deep region is expected to be better represented by the MC-RD calculation than the study performed by Takada et al.¹⁵ Moreover, the thermalization process in our previous study was calculated using an isotropic

kernel, which resulted in an overestimation of the thermal neutron flux near the surface of a cubic phantom by approximately 150%.¹⁶ Compared to these previous works, the calculation accuracy was improved by the adoption of the MC-RD calculation.

In addition, a set of parameters used for the RD calculation in this study was determined in advance using the simplified geometry and adopted for the calculation for cubic and head-shaped phantoms. The calculation result exhibited mostly high consistency with the MC calculation result. Albertson and Niemkiewicz et al. adjusted different parameters to match the RD calculation results with MC calculation results in terms of neutron flux in each energy group in the semi-infinite geometry. They did not verify the accuracy of the RD calculation using the parameters for complex shapes, such as head-shaped phantom.^{17–19}

Recent studies have focused on machine learning for fast dose calculation.²⁷ However, the calculation accuracy depends on the learning data. On the other hand, the MC-RD calculation was conducted based on physical principles, that is, the particle transport equation, as with the conventionally used dose calculation method and can be useful for rapid calculations.

In this study, the MC and RD calculations were conducted using a multi-core central processing unit (i9-10900, Intel Corporation, 10 cores) with a memory size of 128 GB. We evaluated the time required to calculate only the thermal neutron flux in the cubic water phantom with the mesh size of 3 mm by confirming the convergence in the batch-to-batch difference of calculation result with the interval of the same number of particles. In terms of the time required for convergence below 1% of thermal neutron fluxes in the region with a size of $10 \times 10 \times 10 \text{ cm}^3$ near the surface of the phantom, the time required for the MC calculations was approximately 2414 s for the full-continuous-MC calculation and approximately 9 s for the MC-RD calculation. However, the time required for the RD calculation in the MC-RD calculation was approximately 308 s. If the calculation mesh size is increased, the calculation accuracy would be reduced because the extrapolation distance is not correctly reflected in the RD calculation, whereas the calculation time would be shortened. In addition, the time required for the RD calculation would be shortened by improving the specification of the calculator and the optimization of the calculation method. On the other hand, the time required for the MC calculation would be reduced. Therefore, faster calculation is expected by improving the RD calculation method and using smaller mesh sizes.

5 | CONCLUSION

In this study, the MC-RD calculation method was proposed and verified in terms of calculation accuracy by comparing it with the results of the full-continuous-MC

calculation method. The difference between the MC-RD and full-continuous calculation results was attributed to the assumption regarding the angular distribution of neutrons immediately after entering the thermalization process and the limitation of diffusion approximation. However, the MC-RD calculation method is useful for the evaluation of the neutron flux distribution, with the exception of the region near the surface of phantom in BNCT.

ACKNOWLEDGMENTS

This work was supported by JSPS KAKENHI (Grant Number JP20K08078) and JST SPRING (Grant Number JPMJSP2110). We would like to thank Editage (www.editage.jp) for English language editing.

CONFLICT OF INTEREST STATEMENT

The authors declare no conflicts of interest.

REFERENCES

1. Locher GL. Biological effects and therapeutic possibilities of neutron. *Am J Roentgenol.* 1936;36:1-13. https://ia904501.us.archive.org/30/items/sim_ajr-american-journal-of-roentgenology_1936-07_36_1_0/sim_ajr-american-journal-of-roentgenology_1936-07_36_1_0.pdf
2. Barth RF, Vicente MGH, Harling OK, et al. Current status of boron neutron capture therapy of high grade gliomas and recurrent head and neck cancer. *Radiat Oncol.* 2012;7:1-21. doi:10.1186/1748-717X-7-146
3. Fairchild RG, Goodman LJ. Development and dosimetry of an 'epithermal' neutron beam for possible use in neutron capture therapy I. 'Epithermal' neutron beam development. *Phys Med Biol.* 1965;11:491-504. doi:10.1088/0031-9155/10/4/303
4. Suzuki M. Boron neutron capture therapy (BNCT): a unique role in radiotherapy with a view to entering the accelerator-based BNCT era. *Int J Clin Oncol.* 2020;25:43-50. doi:10.1007/s10147-019-01480-4
5. Tanaka H, Sakurai Y, Suzuki M, et al. Characteristics comparison between a cyclotron-based neutron source and KUR-HWNIF for boron neutron capture therapy. *Nucl Instrum Methods Phys Res B.* 2009;267:1970-1977. doi:10.1016/j.nimb.2009.03.095
6. Kato T, Hirose K, Tanaka H, et al. Design and construction of an accelerator-based boron neutron capture therapy (AB-BNCT) facility with multiple treatment rooms at the Southern Tohoku BNCT Research Center. *Appl Radiat Isot.* 2020;156:1-9. doi:10.1016/j.apradiso.2019.108961
7. Kanno H, Nagata H, Ishiguro A, et al. Designation products: boron neutron capture therapy for head and neck carcinoma. *The Oncologist.* 2021;26:e1250-e1255. doi:10.1002/onco.13805
8. Hu N, Tanaka H, Akita K, et al. Accelerator based epithermal neutron source for clinical boron neutron capture therapy. *J Neutron Res.* 2022;24:359-366. doi:10.3233/JNR-220037
9. Sumitomo Heavy Industries, Ltd., World's first BNCT systems as medical device. Accessed July 18, 2023. <https://www.shi.co.jp/english/info/2019/6kgpsq0000002ji0.html>
10. Hu N, Tanaka H, Kakino R, et al. Evaluation of a treatment planning system developed for clinical boron neutron capture therapy and validation against an independent Monte Carlo dose calculation system. *Radiat Oncol.* 2021;16:243. doi:10.1186/s13014-021-01968-2
11. Kumada H, Takada K, Sakurai Y, et al. Development of a multi-modal Monte Carlo based treatment planning system. *Radiat Prot Dosimetry.* 2018;180:286-290. doi:10.1093/rpd/ncx218

12. Sato T, Iwamoto Y, Hashimoto S, et al. Features of Particle and Heavy Ion Transport code System (PHITS) version 3.02. *J Nucl Sci Technol.* 2018;55:684-690. doi:10.1080/00223131.2017.1419890
13. Chen J, Teng YC, Zhong WB, Yang HB, Hong Q, Liu YH. Development of Monte Carlo treatment planning system for BNCT. *J Phys Conf Ser.* 2022;2313:012012. doi:10.1088/1742-6596/2313/1/012012
14. Zhong WB, Chen J, Teng YC, Liu YH. Introduction to the Monte Carlo dose engine COMPASS for BNCT. *Sci Rep.* 2023;13:11965. doi:10.1038/s41598-023-38648-y
15. Takada K, Kumada H, Liem PH, Sakurai H, Sakae T. Development of Monte Carlo based real-time treatment planning system with fast calculation algorithm for boron neutron capture therapy. *Phys Med.* 2016;32:1846-1851. doi:10.1016/j.ejmp.2016.11.007
16. Nojiri M, Takata T, Hu N, Sakurai Y, Suzuki M, Tanaka H. Development and evaluation of dose calculation algorithm with a combination of Monte Carlo and point-kernel methods for boron neutron capture therapy. *Biomed Phys Express.* 2023;9:1-12. doi:10.1088/2057-1976/acc33c
17. Albertson BJ, Blue TE, Niemkiewicz J. An investigation on the use of removal-diffusion theory for BNCT treatment planning: a method for determining proper removal-diffusion parameters. *Med Phys.* 2001;28:1898-1904. doi:10.1118/1.1386424
18. Niemkiewicz J. A study on the use of removal-diffusion theory to calculate neutron distributions for dose determination in boron neutron capture therapy. Ph.D. dissertation, The Ohio State University. 1996. Accessed August 18, 2023. http://rave.ohiolink.edu/etdc/view?acc_num=osu1487934589976468
19. Niemkiewicz J, Blue TE. Removal-diffusion theory for calculation of neutron distributions in BNCT. *Adv Neutron Capture Therapy.* 1993:177-180. doi:10.1007/978-1-4615-2978-1_35
20. Sakurai Y, Kobayashi T. The medical-irradiation characteristics for neutron capture therapy at the Heavy Water Neutron Irradiation Facility of Kyoto University Research Reactor. *Med Phys.* 2002;29:2328-2337. doi:10.1118/1.1509444
21. International Atomic Energy Agency, Current status of neutron capture therapy. IAEA-TECDOC-1223. 2001. Accessed August 25, 2023. https://www-pub.iaea.org/MTCD/Publications/PDF/te_1223_prn.pdf
22. International Atomic Energy Agency. Advances in Boron Neutron Capture Therapy. Accessed August 2, 2023. https://www-pub.iaea.org/MTCD/Publications/PDF/CRCP-BOR-002_web.pdf
23. Lamarsh JR, Baratta AJ. *Introduction to Nuclear Engineering.* 4th ed. Pearson; 2022:598p.
24. Japan Atomic Energy Agency. PHITS Ver. 3.24 User's Manual, English version. Accessed August 25, 2023. <https://phits.jaea.go.jp/manual/manualE-phits324.pdf>
25. Shibata K, Iwamoto O, Nakagawa T, et al. JENDL-4.0: a new library for nuclear science and engineering. *J Nucl Sci Technol.* 2012;1:1-30. doi:10.1080/18811248.2011.971167
26. Meghreblian RV, Holmes DK. *Reactor Analysis.* McGraw-Hill Inc; 1960:180p.
27. Tian F, Zhao S, Geng C, Guo C, Wu R, Tang X. Use of a neural network-based prediction method to calculate the therapeutic dose in boron neutron capture therapy of patients with glioblastoma. *Med Phys.* 2023;1-11. doi:10.1002/mp.16215

How to cite this article: Nojiri M, Takata T, Hu N, Sakurai Y, Suzuki M, Tanaka H. Neutron flux evaluation algorithm with a combination of Monte Carlo and removal-diffusion calculation methods for boron neutron capture therapy. *Med Phys.* 2024;51:3711–3724. <https://doi.org/10.1002/mp.16931>

APPENDIX: GLOSSARY FOR TERMS USED IN EQUATIONS (1)–(10)

ϕ	the neutron flux
$\phi_{u,m}$	the uncollided neutron flux in the energy group m
$\phi_{c,m}$	the collided neutron flux in the energy group m
$S_{0,m}$	the distribution of neutrons terminated in the energy range of the group m in the phantom
$S_{c,n}$	the source intensity for collided neutrons in the group n
C_m	the ratio of the number of neutrons terminated in the energy range of the group m in the phantom
$\Sigma_{ut,m}$	the macroscopic total reaction cross-section depending on the energy spectrum of uncollided neutrons in the energy group m
$\Sigma_{us,m \rightarrow n}$	the macroscopic scattering reaction cross-section in the process where neutrons moderate from the energy group m to n due to the collision with the material, depending on the energy spectrum of uncollided neutrons in the energy group m
$\Sigma_{cs,m \rightarrow n}$	the macroscopic scattering reaction cross-section in the process where neutrons moderate from the energy group m to n due to the collision with the material, depending on the energy spectrum of collided neutrons in the energy group m
$\Sigma_{ca,n}$	the macroscopic absorption reaction cross-section depending on the energy spectrum of collided neutrons in the energy group n
$\Sigma_{cr,n}$	the macroscopic removal cross-section depending on the energy spectrum of collided neutrons in the energy group n
λ_{tr}	mean free path
D_n	the diffusion coefficient for collided neutrons in the energy group n
ϵ_n	the extrapolation distance for collided neutrons in the energy group n
